

# Simulating Three-Flavor Neutrino Oscillations on an NMR Quantum Processor

Gayatri Singh,<sup>\*</sup> Arvind,<sup>†</sup> and Kavita Dorai<sup>‡</sup>

*Department of Physical Sciences, Indian Institute of Science Education & Research Mohali,  
Sector 81 SAS Nagar, Manauli PO 140306 Punjab India.*

Neutrino oscillations can be efficiently simulated on a quantum computer using the Pontecorvo-Maki-Nakagawa-Sakata (PMNS) theory in close analogy to the physical processes realized in experiments. We simulate three-flavor neutrino oscillations on a two-qubit NMR quantum information processor. The three-flavor neutrino states were encoded into the two-qubit system, leaving one redundant basis state (representing an unphysical sterile neutrino). We simulated the neutrino oscillations in different scenarios, including propagation in vacuum and through surrounding matter, and both with and without a CP violating phase  $\delta$  at a Deep Underground Neutrino Experiment (DUNE) baseline distance of  $L = 1285$  km. The oscillation probabilities were obtained after unitarily time evolving the initial flavor state and comparisons were performed between different scenarios. Further, we design and implement an optimized quantum circuit encoding all four parameters (three mixing angles-  $\theta_{12}, \theta_{23}, \theta_{13}$  and one complex phase  $\delta$ ) to implement the PMNS unitary matrix, which relates the flavor and mass eigenstates. The interaction with matter is considered as a perturbation to the vacuum Hamiltonian, and the same quantum circuit is employed with an approximation of two mixing angles ( $\theta_{12}$  and  $\theta_{13}$ ) and mass eigenvalues. Our experimental results match well with numerical simulations and highlight the potential of quantum computers for exploring the physics of neutrino oscillations.

## I. INTRODUCTION

Quantum computers have the potential to outperform their classical counterparts through exponential speed-up [1] and have emerged as powerful tools to address complex problems that are either computationally intractable or challenging to probe experimentally. Quantum simulators [2] can validate theoretical models and predictions of system behavior in inaccessible physical regimes, which makes them a promising approach to investigate problems that remain beyond the reach of current experimental techniques. The increasing interest in quantum simulation is driven by its broad applicability across numerous fields, including high-energy physics [3], quantum chemistry [4], cosmology [5], and condensed matter physics [6, 7]. Recently, quantum simulations have been used to investigate particle physics, covering diverse applications such as heavy-ion collision [8], neutral Kaon [9], Parton distribution inside proton [10], and neutrino-nucleus scattering [11].

The intriguing discovery of neutrino oscillations is a significant breakthrough in elementary particle physics, and points to the inadequacy of the standard model (SM) [12] and paves the way for exploring physics beyond the SM [13]. Weakly interacting, neutrinos emerged as a leading candidate for dark matter [14] and also play a pivotal role in astrophysical phenomena such as the merging of neutron star binaries [15] and core-collapse supernovae [16]. A recent study has demonstrated that neutrino oscillations violate the Leggett-Garg inequality [17], emphasizing their inherent quantum mechan-

ical nature. The idea of the ‘neutrino’ dates back to W. Pauli [18], who introduced it to explain the continuous spectrum observed in beta decay. Later, B. Pontecorvo proposed the idea of neutrino oscillations [19], drawing an analogy to neutral Kaon oscillations, eventually culminating in the theory of neutrino oscillations in vacuum [20]. Later, Maki, Nakagawa, and Sakata proposed the basis misalignment between a neutrino’s flavor and mass eigenstates in 1962 [21]. The propagation of neutrinos in matter was identified by Wolfenstein [22], which is now referred to as the ‘matter effect’ and its physical significance and relevance was provided by Mikheyev and Smirnov [23]. The evolution of the neutrino flavor state is described using the Pontecorvo-Maki-Nakagawa-Sakata (PMNS) matrix, parameterized by three mixing angles ( $\theta_{12}, \theta_{13}$  and  $\theta_{23}$ ,) and one complex phase ( $\delta$ ). Additionally, the mass squared differences ( $\Delta m_{ij}^2 = m_i^2 - m_j^2$ ) are the other three parameters governing neutrino oscillations, where  $m_i$  represents the mass of the  $i$ th neutrino mass eigenstate.

A hybrid algorithm was employed to simulate the time evolution of collective neutrino oscillations, with the time-dependent Hamiltonian being approximated using the Trotter-Suzuki method [24]. The efficiency of various quantum hardware in simulating collective neutrino oscillations was demonstrated on an IBM quantum computer [25–28], trapped ions [29–31] and via quantum walk frameworks [32, 33].

The work presented here is the first experimental simulation of neutrino oscillations on an NMR quantum information processor. We proposed an optimized quantum circuit, which was decomposed into CNOT gates and single-qubit rotations, to implement the PMNS matrix that encodes all four parameters ( $\theta_{12}, \theta_{13}, \theta_{23}, \delta$ ) and implemented it experimentally. For all the computations and experiments, we adopted all the parameters

<sup>\*</sup> ph20015@iisermohali.ac.in

<sup>†</sup> arvind@iisermohali.ac.in

<sup>‡</sup> kavita@iisermohali.ac.in

as provided in [34], including  $\Delta m_{21}^2 = 7.42 \times 10^{-5} \text{eV}^2$ ,  $\Delta m_{31}^2 = 2.510 \times 10^{-3} \text{eV}^2$ ,  $\theta_{12} = 33.45^\circ$ ,  $\theta_{13} = 8.62^\circ$  and  $\theta_{23} = 42.1^\circ$ . We also experimentally simulated the neutrino oscillations with a fixed energy ( $E = 0.5 \text{ GeV}$ ) in the presence of matter, considering potentials  $V = 5 \times 10^{-5} \text{ eV}$  and  $V = 10^{-4} \text{ eV}$ , and compared the results with the vacuum case ( $V = 0 \text{ eV}$ ). Additionally, the impact of the CP-violating phase  $\delta$  was simulated for the long baseline Deep Neutrino Underground Experiment (DUNE) [35] ( $L = 1285 \text{ km}$ ) by varying  $E$ . The results were compared for the vacuum and the matter-interacting scenarios.

Neutrino oscillations occur because of the mismatch between the flavor eigen basis and the mass eigen basis in a three-dimensional Hilbert space, very similar to the case of quarks. PMNS matrices in this case and the CKM matrices in the case of quarks, are special matrices belonging to the group  $SU(3)$  [36, 37]. The study of three-level systems and the structure of  $SU(3)$  has several interesting aspects and we will extend our work to explore some of these directions [38–40].

This paper is organized as follows: the PMNS theory of three-flavor neutrino oscillations is briefly described in Section II, offering a mathematical description of neutrino oscillations in vacuum in Section II A. Section II B outlines the effective Hamiltonian, evolution, mixing angle, and mass eigenvalues for neutrinos interacting with matter. The encoding of three neutrino flavors in a two-qubit system and the quantum circuit for simulating three-flavor neutrino oscillations is described in Section II C. Section III A contains details of the NMR experiments involving initial state preparation, while Section III B describes the simulation of neutrino oscillations encompassing experimental results and analysis for all scenarios, both with and without the CP-violating phase: (i) in vacuum and (ii) interaction with matter. A few conclusions are presented in Section IV.

## II. NEUTRINO OSCILLATIONS AND PMNS THEORY

Lepton mixing is a consequence of the non-correspondence between the basis of the flavor eigenstate  $\{|\nu_e\rangle, |\nu_\mu\rangle, |\nu_\tau\rangle\}$  and the basis of the mass eigenstate  $\{|\nu_1\rangle, |\nu_2\rangle, |\nu_3\rangle\}$  for neutrinos [41, 42]. The existence of this lepton flavor mixing and non-degenerate neutrino masses [20, 43] gives rise to the interesting quantum mechanical phenomenon known as ‘‘Neutrino oscillations’’. The  $SU(3)$  matrix that connects these two sets of bases and thus accounts for misalignment between the mass of a neutrino and its flavor eigenstates is known as the Pontecorvo-Maki-Nakagawa-Sakata (PMNS) matrix ( $U_{\text{PMNS}}$ ) [21, 42].

A neutrino with flavor  $\alpha$  and momentum  $p$  is described using the PMNS matrix in terms of the mass eigen states as

$$|\nu_\alpha\rangle = U_{\alpha j}^* |\nu_j\rangle \quad (1)$$

where,  $\alpha = e, \mu, \tau$  and  $i = 1, 2, 3$ , and  $U_{\alpha j}^*$  is  $\alpha j$ th element of complex conjugate of  $U_{\text{PMNS}}$  matrix (For antineutrinos, we have:  $|\bar{\nu}_\alpha\rangle = U_{\alpha j} |\bar{\nu}_j\rangle$ ). For Dirac neutrinos, the PMNS matrix is completely characterized by three mixing angles  $\theta_{12}, \theta_{13}, \theta_{23}$  and a complex phase  $\delta$  for charge conjugation and parity reversal (CP) symmetry violations as:

$$U_{\text{PMNS}} = \begin{pmatrix} U_{e1} & U_{e2} & U_{e3} \\ U_{\mu 1} & U_{\mu 2} & U_{\mu 3} \\ U_{\tau 1} & U_{\tau 2} & U_{\tau 3} \end{pmatrix} \equiv U_{\text{PMNS}}(\theta_{12}, \theta_{23}, \theta_{13}, \delta) \\ = \begin{pmatrix} 1 & 0 & 0 \\ 0 & \cos \theta_{23} & \sin \theta_{23} \\ 0 & -\sin \theta_{23} & \cos \theta_{23} \end{pmatrix} \begin{pmatrix} \cos \theta_{13} & 0 & \sin \theta_{13} e^{-i\delta} \\ 0 & 1 & 0 \\ -\sin \theta_{13} e^{i\delta} & 0 & \cos \theta_{13} \end{pmatrix} \\ \begin{pmatrix} \cos \theta_{12} & \sin \theta_{12} & 0 \\ -\sin \theta_{12} & \cos \theta_{12} & 0 \\ 0 & 0 & 1 \end{pmatrix} \quad (2)$$

### A. Neutrino Oscillations in Vacuum

Since neutrinos are relativistic particles, the energy of the  $j$ -th mass eigenstate with momentum  $p$  and mass  $m_j$  is approximated in vacuum as  $E_j = pc + \frac{m_j^2 c^4}{2E}$ . In the PMNS framework, in order to evaluate the time evolution of an initial flavor eigen state  $|\nu_\alpha(0)\rangle$  (at  $t = 0$ ), we will have to first expand it in the mass basis, time evolve each mass eigen state and then re-express the result in the flavor basis as:

$$|\psi(t)\rangle = U_{\alpha j}^* e^{-iE_j t/\hbar} U_{\beta j} |\nu_\beta(0)\rangle \quad (3)$$

which in general involve all the three flavors. In neutrino oscillation experiments, the propagation time  $t$  is not directly observed, but is instead replaced by the known distance  $L$  between the source and the detector, leading to the substitution of  $t$  by  $L/c$ . In a matrix representation, we can express Eqn. 3 as:

$$|\psi(t)\rangle = U_{\text{PMNS}} M(t) U_{\text{PMNS}}^\dagger |\nu_\beta(0)\rangle \quad (4)$$

with  $\hbar = c = 1$ ,

$$M(t) = \begin{pmatrix} 1 & 0 & 0 \\ 0 & e^{-i\frac{\Delta m_{21}^2 L}{2E}} & 0 \\ 0 & 0 & e^{-i\frac{\Delta m_{31}^2 L}{2E}} \end{pmatrix}$$

where  $\Delta m_{ij}^2 = m_i^2 - m_j^2$  denotes neutrino mass squared difference and

$$\frac{\Delta m_{ij}^2 L}{2E} = 2 \times 1.27 \times \Delta m_{ij}^2 (\text{eV}^2) \frac{L(\text{km})}{E(\text{GeV})}$$

The probability of detection of neutrino flavor  $\nu_\beta$  from  $\nu_\alpha$  is obtained as

$$P_{\nu_\alpha \rightarrow \nu_\beta} = |\langle \nu_\beta | \psi(t) \rangle|^2 = \sum_{i,j} U_{\alpha i}^* U_{\beta i} U_{\alpha j} U_{\beta j}^* e^{-i\frac{\Delta m_{ij}^2 L}{2E}} \quad (5)$$

The above expression indicates that the phases of neutrino oscillations are determined by the experiment-dependent quantities  $L$  and  $E$ . For large  $L/E$ , neutrino oscillations are experimentally accessible even for tiny masses of neutrinos. The PMNS matrix governing neutrino oscillations is also characterized by a complex phase  $\delta$ , that leads to the dependence of the oscillations on  $\delta$ , enabling the observation of CP symmetry violation as the neutrino and the anti-neutrino oscillate with different probabilities.

## B. Neutrino Oscillations in Matter

The modification in the mixing of neutrinos during propagation in matter was first observed by Wolfenstein [22] and governed by a modified Hamiltonian which contains two terms [44, 45]: the vacuum Hamiltonian in the flavor basis  $H_0$ , and the potential term arising due to interaction of neutrinos in matter  $V_m$  [46]. The modified Hamiltonian is defined as:

$$H = \underbrace{\frac{1}{2E} U_{\text{PMNS}} \begin{pmatrix} 0 & 0 & 0 \\ 0 & \Delta m_{21}^2 & 0 \\ 0 & 0 & \Delta m_{31}^2 \end{pmatrix} U_{\text{PMNS}}^\dagger}_{H_0} + \underbrace{\begin{pmatrix} V & 0 & 0 \\ 0 & 0 & 0 \\ 0 & 0 & 0 \end{pmatrix}}_{V_m} \quad (6)$$

where  $V = \sqrt{2} G_F N_e$  represents the Wolfenstein matter potential [22], which is induced by coherent forward scattering of neutrinos on electrons in matter;  $G_F$  is the Fermi coupling constant, and  $N_e$  is the number density of electrons in matter. The matter interaction term (potential term) can be regarded as a perturbation to the vacuum Hamiltonian.

Due to the presence of this interaction term, the mass eigenstates governing neutrino propagation in matter differ from the mass eigenstates  $|\nu_j\rangle$  observed in vacuum. Instead, they are matter eigenstates  $|\tilde{\nu}_j\rangle$ , which connects to the flavor eigenstates through the matter mixing matrix  $\tilde{U}_{\text{PMNS}}$ . This matrix encodes the modified mixing angles and diagonalizes the Hamiltonian while preserving a similar form to the vacuum case as:

$$H = \frac{1}{2E} \tilde{U}_{\text{PMNS}} \begin{pmatrix} 0 & 0 & 0 \\ 0 & \Delta \tilde{m}_{21}^2 & 0 \\ 0 & 0 & \Delta \tilde{m}_{31}^2 \end{pmatrix} \tilde{U}_{\text{PMNS}}^\dagger \quad (7)$$

where  $\tilde{m}_{21}^2$  and  $\tilde{m}_{31}^2$  are mass squared differences for matter interactions [44].

$$\begin{aligned} \Delta \tilde{m}_{21}^2 &= \Delta m_{21}^2 \sqrt{(\cos 2\theta_{12} - \epsilon_1)^2 + (\sin 2\theta_{12} \cos 2\phi_{13})^2} \\ \Delta \tilde{m}_{31}^2 &= \frac{3}{4} \Delta m_{ee}^2 \sqrt{(\cos 2\theta_{13} - \epsilon_2)^2 + \sin^2 2\theta_{13}} \\ &\quad + \frac{1}{4} (\Delta m_{ee}^2 + a) + \frac{1}{2} (\Delta \tilde{m}_{21}^2 - \Delta m_{21}^2 \cos 2\theta_{12}) \end{aligned} \quad (8)$$

with

$$\begin{aligned} \epsilon_1 &= \frac{a}{\Delta m_{21}^2} \cos^2(\phi_{13} + \theta_{13}) + \Delta m_{ee}^2 \frac{\sin^2 \phi_{13}}{\Delta m_{21}^2} \\ \epsilon_2 &= a / \Delta m_{ee}^2 \\ \Delta m_{ee}^2 &= \Delta m_{31}^2 \cos^2 \theta_{12} + \Delta m_{32}^2 \sin^2 \theta_{12} \\ a &= 2EV \approx \frac{V(\sim 10^{-4} \rho_m)}{(\text{eV})} \frac{E}{(\text{GeV})} \text{eV}^2 \end{aligned}$$

where  $\rho_m(\text{g/cm}^3)$  is the density of matter and  $\Delta m_{ee}^2$  is the effective mass squared difference for electron flavor [47]. The matter mixing matrix  $\tilde{U}_{\text{PMNS}} \equiv \tilde{U}_{\text{PMNS}}(\tilde{\theta}_{12}, \tilde{\theta}_{23}, \tilde{\theta}_{13}, \tilde{\delta})$  is characterized by modified  $\tilde{\theta}_{ij}$  and  $\tilde{\delta}$  as defined in [44].

$$\begin{aligned} \cos 2\tilde{\theta}_{13} &= \frac{\cos 2\theta_{13} - \epsilon_2}{\sqrt{(\cos 2\theta_{13} - \epsilon_2)^2 + \sin^2 2\theta_{13}}} \\ \cos 2\tilde{\theta}_{12} &= \frac{\cos 2\theta_{12} - \epsilon_1}{\sqrt{(\cos 2\theta_{12} - \epsilon_1)^2 + (\sin 2\theta_{12} \sin 2\phi_{13})^2}} \quad (9) \\ \tilde{\theta}_{23} &\equiv \theta_{23} \\ \tilde{\delta} &\equiv \delta \end{aligned}$$

## C. Simulating Three-Flavor Neutrino Oscillations in a Two-Qubit Subspace

To simulate three-flavor neutrino oscillations on a two-qubit system, we mapped the three neutrino flavor eigenstates  $\{|\nu_e\rangle, |\nu_\mu\rangle, |\nu_\tau\rangle\}$  to the orthogonal states of a two-qubit system. The remaining basis is assigned to represent the fourth neutrino flavor, i.e., the light sterile neutrino [48]  $|\nu_\chi\rangle$  as:

$$|\nu_e\rangle = \begin{pmatrix} 1 \\ 0 \\ 0 \\ 0 \end{pmatrix} \quad |\nu_\mu\rangle = \begin{pmatrix} 0 \\ 1 \\ 0 \\ 0 \end{pmatrix} \quad |\nu_\tau\rangle = \begin{pmatrix} 0 \\ 0 \\ 1 \\ 0 \end{pmatrix} \quad |\nu_\chi\rangle = \begin{pmatrix} 0 \\ 0 \\ 0 \\ 1 \end{pmatrix} \quad (10)$$

A sterile neutrino is a neutral fermion that does not participate in weak interactions, and in our work, we have considered sterile neutrinos to be physically decoupled. Thus, the PMNS matrix becomes a  $4 \times 4$  unitary matrix connecting flavor eigenstates  $\{|\nu_e\rangle, |\nu_\mu\rangle, |\nu_\tau\rangle, |\nu_\chi\rangle\}$  to mass eigenstates  $\{|\nu_1\rangle, |\nu_2\rangle, |\nu_3\rangle, |\nu_4\rangle\}$  and Eqn. 2 gets modified to:

$$U_{\text{PMNS}} = \begin{pmatrix} U_{e1} & U_{e2} & U_{e3} & 0 \\ U_{\mu 1} & U_{\mu 2} & U_{\mu 3} & 0 \\ U_{\tau 1} & U_{\tau 2} & U_{\tau 3} & 0 \\ 0 & 0 & 0 & 1 \end{pmatrix} \quad (11)$$

and  $M(t)$  is modified to:

$$M(t) = \begin{pmatrix} 1 & 0 & 0 & 0 \\ 0 & e^{-i \frac{\Delta m_{21}^2 L}{2E}} & 0 & 0 \\ 0 & 0 & e^{-i \frac{\Delta m_{31}^2 L}{2E}} & 0 \\ 0 & 0 & 0 & e^{-i \Phi_{\text{ab}}} \end{pmatrix} \quad (12)$$

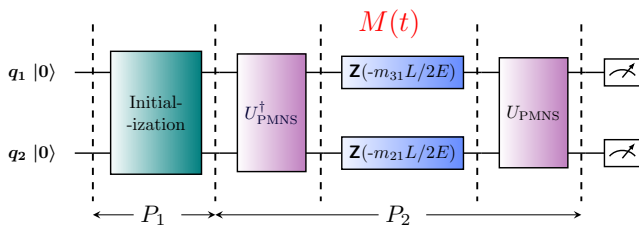


FIG. 1. Quantum circuit using the PMNS framework for three-flavor neutrino oscillations, starting with flavor state initialization on a two-qubit system.

The phase  $\Phi_{ab}$  can be chosen conveniently without impacting observable quantities, offering phase freedom in the  $\nu_\chi$  basis. It enables the simulation of the time evolution operator  $M(t)$  by employing only single qubit  $z$ -rotations.

Figure 1 illustrates the quantum circuit designed for simulating three-flavor neutrino oscillations. Initially, the system is initialized in one of the flavor states  $\{|\nu_e\rangle, |\nu_\mu\rangle, |\nu_\tau\rangle\}$ . Subsequently, the PMNS matrix is employed to transform to the mass basis, as outlined in Eqn. 1. The state then undergoes evolution according to Eqn. 3, followed by another transformation from the mass basis back to the flavor basis using the PMNS matrix.

A new circuit using controlled rotations was designed to encode the PMNS matrix in three and higher dimensions and to incorporate the CP violating phase [26]. According to this novel circuit, a two-qubit system necessitates three controlled rotations and two CNOT gates to implement the PMNS matrix encoding four parameters (three mixing angles and one complex phase). While this circuit is efficient and provides physical insights into all four parameters, further optimization is required for implementation on experimental platforms such as NMR quantum processors, where increased gate complexity introduces decoherence effects, significantly impacting fidelity. Therefore, we introduced an optimized quantum circuit utilizing four CNOT gates combined with single-qubit rotations to implement the PMNS matrix on a two-qubit system (Figure 2). For simulations of neutrino oscillations in the presence of matter, the same quantum circuit is used (Figure 1) with modified parameters (Eqn. 9) ( $\tilde{\theta}_{12}, \tilde{\theta}_{13}, \tilde{\theta}_{23}, \tilde{\delta}, \tilde{m}_{21}, \tilde{m}_{31}$ ).

### III. EXPERIMENTAL IMPLEMENTATION ON AN NMR QUANTUM PROCESSOR

#### A. Initial State Preparation

Neutrino oscillations were simulated using a two-qubit NMR quantum information processor. All the experiments were performed on a Bruker DRX Avance-III 600 MHz NMR spectrometer equipped with a standard 5 mm QXI probe at room temperature  $\approx 300\text{K}$ , with the power

level set to be 18.14 W in all the experiments. The qubits are encoded by the two protons of cytosine molecule dissolved in deuterated solvent  $\text{D}_2\text{O}$ . The molecular structure and molecular parameters are listed in Figure 3. The Hamiltonian of a two spin-1/2 system, under weak coupling approximation, in the rotating frame rotating with a frequency  $\omega_{rf}$  is expressed as [49]

$$\mathcal{H} = -\sum_{i=1}^2 (\omega_i - \omega_{rf}) I_z^i + 2\pi \sum_{i,j=1, i>j}^2 J_{ij} I_z^i I_z^j \quad (13)$$

where  $\omega_i = 2\pi\nu_i$  is the Larmor frequency and  $I_z^i$  is the  $z$  component of spin angular momentum of  $i$ th nuclei. We used the spatial averaging technique [49] to initialize the system in a pseudo-pure state (PPS)  $|00\rangle$  with the corresponding density operator

$$\rho_{00} = \frac{1-\eta}{2^2} \mathbb{I}_{4\times 4} + \eta|00\rangle\langle 00| \quad (14)$$

where  $\eta \sim 10^{-5}$  is the thermal polarization and  $\mathbb{I}_{4\times 4}$  is the Identity operator. We employed the Uhlmann-Jozsa fidelity measure [50, 51] which calculates the projection between theoretically expected density matrix  $\rho_{\text{th}}$  and experimentally reconstructed density matrix  $\rho_{\text{exp}}$ , to measure the fidelity of an experimentally reconstructed density matrix as:

$$\mathcal{F} = \left[ \text{Tr} \left[ \sqrt{\sqrt{\rho_{\text{th}}} \rho_{\text{exp}} \sqrt{\rho_{\text{th}}}} \right] \right]^2 \quad (15)$$

In this work, we used the constrained convex optimization based reduced state tomography method [52] to reconstruct a physically valid density matrix. We used the NMR pulse sequence given in Reference [53] to prepare the PPS from the thermal equilibrium state. The PPS is then experimentally tomographed with fidelity  $\mathcal{F} = 0.997 \pm 0.0012$  using a set of tomographic pulses  $\{II, IX, IY, XX\}$ , where,  $X(Y)$  denotes a spin-selective  $\pi/2$  rotation along  $x(y)$  axis and  $I$  is the identity operation (do nothing). All single-qubit selective excitations with duration ranging from approximately 350 to 700  $\mu\text{s}$  and an average fidelity  $\geq 0.999$  were optimized using the Gradient Ascent Pulse Engineering (GRAPE) algorithm [54–56] and were crafted to be robust against rf inhomogeneity.

#### B. Experimental Simulation of Neutrino Oscillations

The quantum circuit depicted in Figure 1 is implemented on NMR quantum processor utilizing GRAPE-optimized radio-frequency pulses. For experimental implementation  $P_1$  pulse with duration  $\sim 650\text{-}700 \mu\text{s}$  is used for state initialization and a single GRAPE-optimized pulse  $P_2$  was crafted for entire unitary operation  $U_{\text{PMNS}} M(t) U_{\text{PMNS}}^\dagger$  with a pulse duration ranging

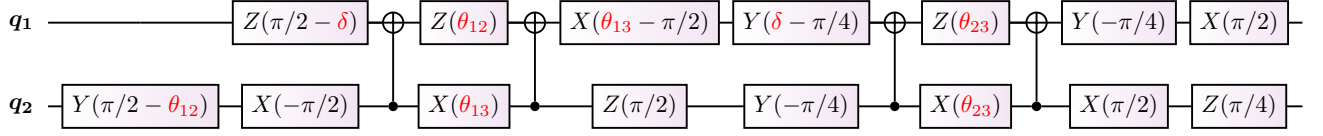


FIG. 2. Optimized quantum circuit designed to implement the PMNS matrix on a two-qubit system, encoding all four parameters  $\{\theta_{12}, \theta_{23}, \theta_{13}, \delta\}$ .

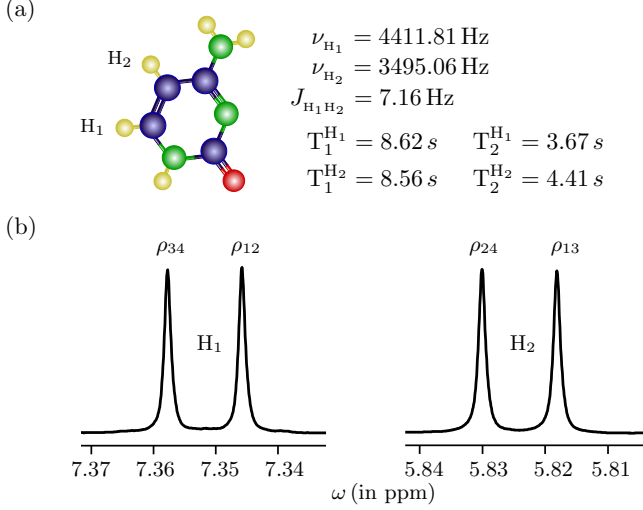


FIG. 3. (a) Molecular structure of cytosine molecule, along with its Hamiltonian parameters, including Larmor frequencies, scalar J-coupling and relaxation times  $T_1$  and  $T_2$  for Hydrogen nuclei  $H_1$  and  $H_2$ . Purple, green, red, and yellow balls represent the carbon, nitrogen, oxygen, and hydrogen nuclei, respectively. (b) NMR spectra (real: absorption mode) corresponding to the hydrogen nuclei of cytosine molecule obtained by applying a  $\pi/2$  readout pulse on the thermal equilibrium state. The spectral lines of each qubit, which represent the elements  $\rho_{12}$ ,  $\rho_{34}$ ,  $\rho_{13}$ , and  $\rho_{24}$  of the density matrix  $\rho$ , are delineated in the spectrum.

from 5000 to 18000  $\mu\text{s}$  for various  $L/E$  value in case of vacuum and matter interaction. After implementing the entire unitary operation (Eqn. 4), the resulting density matrix can be expressed generally as

$$\rho = \begin{pmatrix} \rho_{11} & \rho_{12} & \rho_{13} & \rho_{14} \\ \rho_{12}^* & \rho_{22} & \rho_{23} & \rho_{24} \\ \rho_{13}^* & \rho_{23}^* & \rho_{33} & \rho_{34} \\ \rho_{14}^* & \rho_{24}^* & \rho_{34}^* & \rho_{44} \end{pmatrix} \quad (16)$$

Following this, the diagonal entries of  $\rho$  corresponds to the oscillation probabilities as  $P(\nu_\alpha \rightarrow \nu_e) = \rho_{11}$ ,  $P(\nu_\alpha \rightarrow \nu_\mu) = \rho_{22}$  and  $P(\nu_\alpha \rightarrow \nu_\tau) = \rho_{33}$ .

The NMR spectra of cytosine molecule (Figure 3) include NMR signal for protons  $H_1$  and  $H_2$ , each consists of two spectral peaks corresponding to the transitions associated with specific density matrix elements, known as readout elements:  $\rho_{12}, \rho_{34}$  from spectrum corresponding to  $H_1$  and  $\rho_{13}, \rho_{24}$  from spectrum corresponding to  $H_2$ . The diagonal elements of the density matrix, however,

are not directly observable. To determine them, one has to either reconstruct the full density matrix or the expectation values  $\langle I_z^1 \rangle$ ,  $\langle I_z^2 \rangle$  and  $\langle I_z^1 I_z^2 \rangle$  operators should be evaluated. As discussed in the previous section, four tomographic pulses are required to reconstruct the full experimental density matrix. Additionally, to directly calculate the expectation values, we have to map to the local z-magnetization of one of the qubits followed by the implementation of the corresponding unitary operations to obtain each expectation value [57].

Rather than employing the aforementioned methods, we have embraced an alternative approach. Through the acquisition of NMR signals from  $H_1$  and  $H_2$  following the implementation of only two acquisition pulses  $\{YI, IY\}$ , we can obtain the diagonal entries  $\rho_{11}, \rho_{22}$  and  $\rho_{33}$  for each  $L/E$  values. After implementing acquisition pulse  $YI$  and  $IY$ , the state is mapped into another state as  $\rho^1 = YI \cdot \rho \cdot YI^\dagger$  and  $\rho^2 = IY \cdot \rho \cdot IY^\dagger$  respectively. The line intensities in the absorption mode of NMR spectra (real part of readout element) of these mapped states contain information about the diagonal entries of  $\rho$  and it can be mathematically expressed as

$$\begin{aligned} \rho_{11} &= (1 + 2(\rho_{13}^1 + \rho_{24}^1) + 4\rho_{12}^2)/4 \\ \rho_{22} &= (1 + 2(\rho_{13}^1 + \rho_{24}^1) - 4\rho_{12}^2)/4 \\ \rho_{33} &= (1 - 2(\rho_{13}^1 + \rho_{24}^1) + 4\rho_{34}^2)/4 \end{aligned} \quad (17)$$

where,  $\rho_{jk}^i$  is the spectral line intensity of mapped state  $\rho^i$  with respect to the readout element  $jk$ .

Figure 4 illustrates the vacuum oscillations in three flavor neutrino system, without incorporating CP violating phase  $\delta$ , focussing on a smaller  $L/E$  range, where oscillations are approximately two flavor dominant. The plots show the probability of detecting final neutrino flavor state  $\nu_\alpha$  as a function of standard scale  $L(\text{km})/E(\text{GeV})$  starting from three different initial states: electron neutrino (Figure 4(a)), muon neutrino (Figure 4(b)) and tau neutrino (Figure 4(c)). The final neutrino state  $\nu_\alpha : \nu_e, \nu_\mu$  and  $\nu_\tau$  are visually distinguished by the blue, green and red colors respectively. Solid lines correspond to results from numerical simulations, while experimental data is represented by dots with error bars.

In the case of interaction with matter, we treated the potential term as a perturbation to the vacuum Hamiltonian and diagonalized the total Hamiltonian to maintain the same form as in the vacuum scenario. As a result, we implemented the identical quantum circuit illustrated in Figure 1, 2 with modified parameters

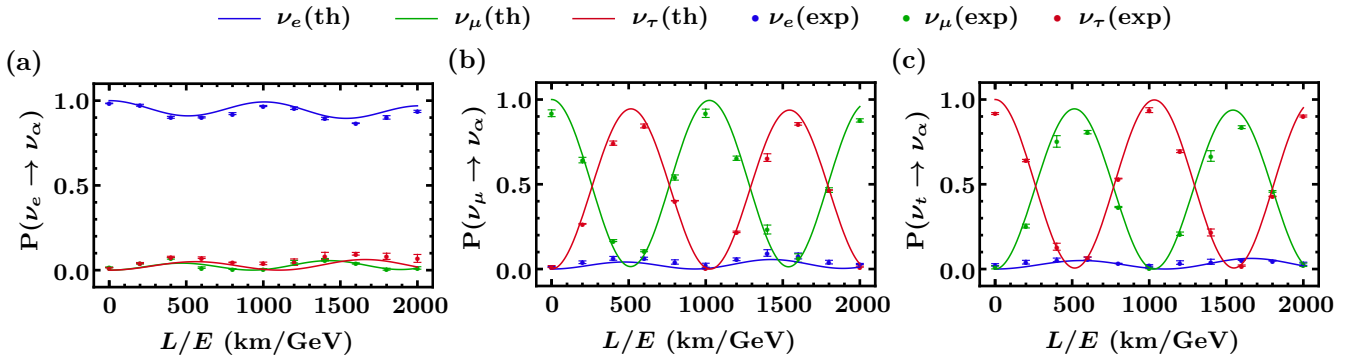


FIG. 4. The three-flavor neutrino oscillation probability as a function of standard scale  $L(\text{km})/E(\text{GeV})$ : solid lines represent the numerical simulations and dots with error bars corresponds to the experimental simulations on NMR for various initial states: (a) electron neutrino, (b) muon neutrino, and (c) tauon neutrino. The colors blue, green, and red represent the final states  $\nu_\alpha$ :  $\nu_e, \nu_\mu$  and  $\nu_\tau$ , respectively.

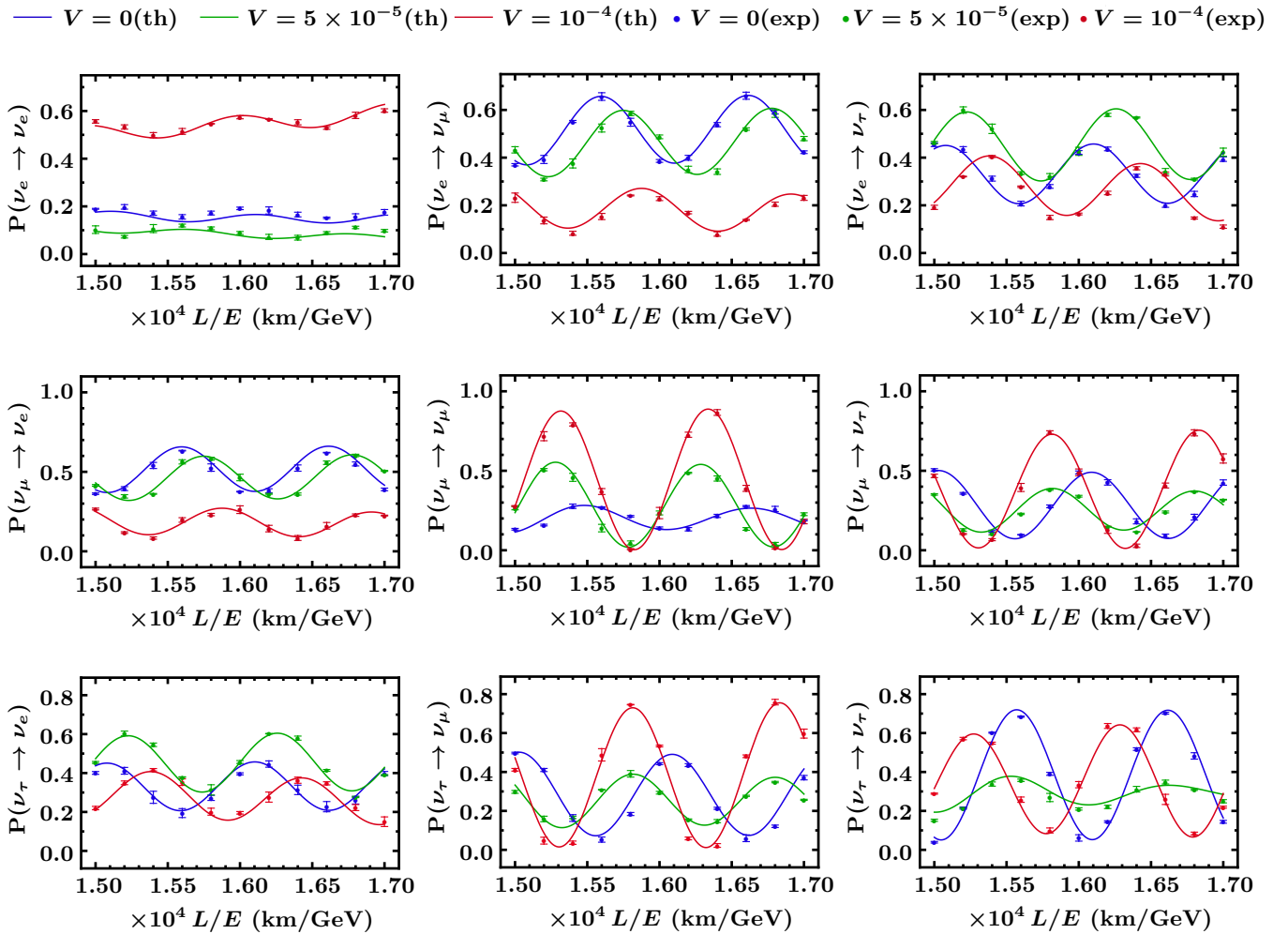


FIG. 5. Comparison of neutrino oscillations probability of as a function of standard scale  $L(\text{km})/E(\text{GeV})$  with energy  $E = 0.5$  GeV in presence of matter with potential  $V = 0$  eV (blue),  $V = 5 \times 10^{-5}$  eV (green) and  $V = 10^{-4}$  eV (red). In this illustration, each row corresponds to the initial state, and each column corresponds to the final state of the neutrino  $\nu_e, \nu_\mu$  and  $\nu_\tau$  respectively. The solid curve depicts the numerically simulated results, while the dots represent the experimentally simulated results.

$(\tilde{\theta}_{12}, \tilde{\theta}_{13}, \tilde{\theta}_{23}, \tilde{m}_{21}, \tilde{m}_{31})$  and  $\delta = 0$  for different value of  $V$ . We selected three distinct values for  $V = 0, 5 \times 10^{-5},$



and  $10^{-4}$  eV to examine the impact of the presence of matter interaction and simulated neutrino oscillations for all three neutrino states as the initial state. The experimentally simulated and numerically simulated oscillation probabilities starting with different initial states for  $\delta = 0$  are depicted in Figure 5. In this figure, row represents the initial state  $(\nu_e, \nu_\mu, \nu_\tau)$  and column represents the final state  $(\nu_e, \nu_\mu, \nu_\tau)$ . For instance, the plot in the second column of the first row illustrates the oscillation probability of detecting  $\nu_\mu$  starting from an initial state of  $\nu_e$  under different potentials.

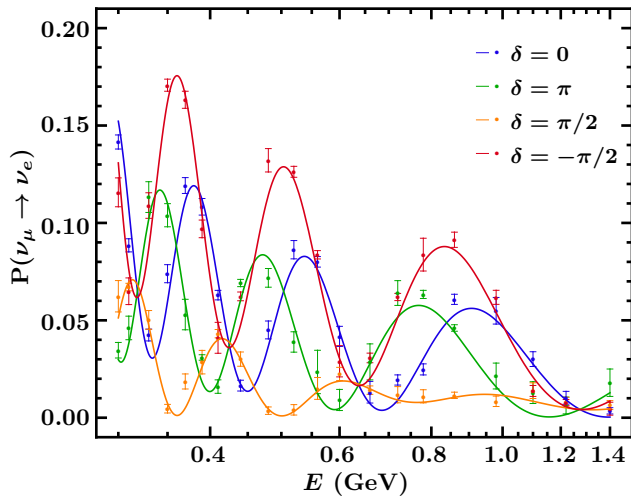


FIG. 6. The oscillations probability of  $\nu_\mu \rightarrow \nu_e$  as a function of  $E$  (GeV) across the DUNE baseline length of 1298 km is evaluated for different CP-violating phases:  $\delta = 0, \pi/2, \pi$ , and  $-\pi/2$ , under vacuum conditions ( $V = 0$  eV). The numerical simulations are depicted by solid curves, while the dots with error bars represent the experimental data.

We also showcased the efficacy of the quantum circuit in implementing the PMNS matrix, incorporating a CP-violating phase  $\delta \neq 0$ . Figure 6 illustrates the oscillation probabilities of  $\nu_e$  appearance starting with the initial state of  $\nu_\mu$  as a function of energy  $E$  (GeV) over a baseline length of  $L = 1298$  km (reflecting DUNE experimental configuration). In this plot, dots with error bars represents the experimental data, while the solid lines are the numerical results for different values of  $\delta = 0, \pi/2, \pi, -\pi/2$ . CP violating phase  $\delta$  alters the atmospheric oscillations by introducing both a phase shift and a constant offset, with the oscillation probability containing terms proportional to  $\sin \delta$  and  $\cos \delta$ . These terms influence the interference between mass eigenstates as they propagate, leading to constructive interference for  $\delta = -\pi/2$  and destructive interference in case of  $\delta = \pi/2$  (Figure 6). Although both  $\delta = 0$  and  $\pi$  correspond to the scenario without CP violation, since the Hamiltonian is real, the oscillations probabilities differ in these two cases due to distinct interference.

We then experimentally simulated the oscillations with the initial state of the muon neutrino  $\nu_\mu$  for  $V = 10^{-4}$  eV at CP-violating phase  $\delta = 0$  and  $-\pi/2$ , and com-

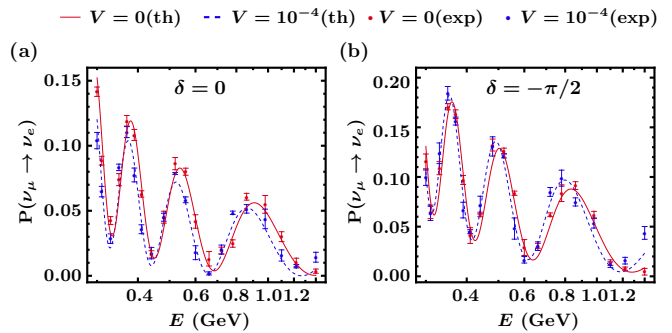


FIG. 7. A comparative study of oscillation probabilities of  $\nu_\mu \rightarrow \nu_e$  as a function of energy ( $E$  in GeV) for a baseline length of 1298 km (which is the distance between the source and the detector in the DUNE experiment). The comparison was made for oscillations with potential  $V = 0$  eV and  $V = 10^{-4}$  eV, considering two different values of the CP-violating phase  $\delta = 0$  and  $\delta = -\pi/2$ . The results are illustrated by solid red curves for  $V = 0$  eV and dashed green curves for  $V = 10^{-4}$  eV in numerical simulations, while experimental data are represented by dots with error bars.

pared the oscillation probabilities of  $\nu_e$  appearance with the vacuum scenario ( $V = 0$  eV). Figure 7 illustrates this comparison. In the context of the DUNE distance, the primary factor influencing oscillation probabilities is the change in the angle  $\theta_{13}$ . However, it is noteworthy that the change in the angle  $\theta_{13}$  is relatively small, which results in small differences between vacuum and matter oscillations, but exhibit qualitatively similar characteristics [44].

All the experimental simulations are in good agreement with the numerical simulations, effectively demonstrating an interplay between neutrino mixing parameter and the complex phase  $\delta$  in three-flavor neutrino oscillations. This highlights the successful implementation of the PMNS framework to simulate neutrino oscillations on an NMR quantum processor.

#### IV. CONCLUSION

We successfully demonstrated the quantum simulation of three-flavor neutrino oscillations using PMNS theory on a subspace of a two-qubit NMR quantum information processor. We highlighted the efficacy of the proposed quantum circuit for implementing the PMNS matrix encoding the parameters,  $\theta_{12}, \theta_{13}, \theta_{23}$ , and  $\delta$ . This circuit employs single rotations and four CNOT gates and is experimentally feasible to implement using GRAPE-optimized rf pulses, thus reducing circuit complexity and errors. Furthermore, we presented an alternative approach (specific to the NMR platform) to directly obtain probabilities from NMR spectra, obviating the need for reconstructing the full density matrix by computing expectation values of  $\langle I_z^1 \rangle, \langle I_z^2 \rangle$ , and  $\langle I_z^1 I_z^2 \rangle$  operators. Our experimental results closely align with the theoretic-

cal simulations of PMNS theory, encompassing scenarios with and without CP-violating phase  $\delta$  for both, oscillations in vacuum and interaction with matter. A comparative analysis was made for the vacuum by incorporating CP phase  $\delta = 0, \pi/2, \pi$  and  $-\pi/2$ . We showcased the performance of the optimized quantum circuit by employing it for matter interaction case, incorporating the CP-violating phase and then comparing it with the vacuum scenario.

The advantage of quantum simulators beyond their classical counterparts becomes apparent when addressing complex scenarios, such as collective neutrino oscillations, and correlations in neutrino-neutrino interactions, which is a many-body problem with a computational cost that scales exponentially with the number of neutrinos [3]. Moreover, using quantum simulations, out-of-equilibrium flavor dynamics can be explored in regimes inaccessible by classical approaches [30]. Quantum computers have the potential to explore scenarios beyond the

Standard Model, such as the existence of sterile neutrinos to explain experimental anomalies that cannot be accounted for by the three-flavor oscillation framework and to probe properties of neutrinos beyond their masses and mixing, or interactions that deviate from weak interactions [58]. Our study explores the potential of quantum simulators such as NMR quantum processors as a valuable tool to understand high-energy physics phenomena, shedding light on aspects that present challenges for direct experimental observation.

## ACKNOWLEDGMENTS

All experiments were performed on a Bruker DRX Avance-III 600 MHz FT-NMR spectrometer at the NMR Research Facility at IISER Mohali. G.S. acknowledges University Grants Commission (UGC), India for financial support.

- 
- [1] R. P. Feynman, *Int. J. Theor. Phys.* **21**, 467 (1982).  
 [2] S. Lloyd, *science* **273**, 1073 (1996).  
 [3] C. W. Bauer and et. al., *PRX Quantum* **4**, 027001 (2023).  
 [4] I. Kassal, J. D. Whitfield, A. Perdomo-Ortiz, M.-H. Yung, and A. Aspuru-Guzik, *Annu. Rev. Phys. Chem.* **62**, 185 (2011), pMID: 21166541.  
 [5] P. Mocz and A. Szasz, *Astrophys. J.* **910**, 29 (2021).  
 [6] X. Peng, J. Du, and D. Suter, *Phys. Rev. A* **71**, 012307 (2005).  
 [7] A. S. Kazmina, I. V. Zalivako, A. S. Borisenko, N. A. Nemkov, A. S. Nikolaeva, I. A. Simakov, A. V. Kuznetsova, E. Y. Egorova, K. P. Galstyan, N. V. Semenina, A. E. Korolkov, I. N. Moskalenko, N. N. Abramov, I. S. Besedin, D. A. Kalacheva, V. B. Lubsanov, A. N. Bolgar, E. O. Kiktenko, K. Y. Khabarova, A. Galda, I. A. Semerikov, N. N. Kolachevsky, N. Maleeva, and A. K. Fedorov, *Phys. Rev. A* **109**, 032619 (2024).  
 [8] W. A. de Jong, M. Metcalf, J. Mulligan, M. Płoskoń, F. Ringer, and X. Yao, *Phys. Rev. D* **104**, L051501 (2021).  
 [9] R. Bertlmann, W. Grimus, and B. Hiesmayr, *Phys. Lett. A* **289**, 21 (2001).  
 [10] A. Pérez-Salinas, J. Cruz-Martinez, A. A. Alhajri, and S. Carrazza, *Phys. Rev. D* **103**, 034027 (2021).  
 [11] A. Roggero, A. C. Y. Li, J. Carlson, R. Gupta, and G. N. Perdue, *Phys. Rev. D* **101**, 074038 (2020).  
 [12] T.-P. Cheng, L.-F. Li, and D. Gross, *Physics Today - PHYS TODAY* **38** (1985), 10.1063/1.2814821.  
 [13] R. W. Rasmussen, L. Lechner, M. Ackermann, M. Kowalski, and W. Winter, *Phys. Rev. D* **96**, 083018 (2017).  
 [14] L. Bergström, *New J. Phys.* **11**, 105006 (2009).  
 [15] D. Radice, A. Perego, K. Hotokezaka, S. A. Fromm, S. Bernuzzi, and L. F. Roberts, *Astrophys. J.* **869**, 130 (2018).  
 [16] G. M. Fuller, W. C. Haxton, and G. C. McLaughlin, *Phys. Rev. D* **59**, 085005 (1999).  
 [17] J. A. Formaggio, D. I. Kaiser, M. M. Murskyj, and T. E. Weiss, *Phys. Rev. Lett.* **117**, 050402 (2016).  
 [18] W. Pauli, *History [of neutrino physics]* (Cambridge University Press, United Kingdom, 1991).  
 [19] B. Pontecorvo, *Zh. Eks Teor. Fiz.* **33**, 549 (1957).  
 [20] B. Pontecorvo, *Zh. Eksp. Teor. Fiz.* **53**, 1717 (1967).  
 [21] Z. Maki, M. Nakagawa, and S. Sakata, *Prog. Theor. Phys.* **28**, 870 (1962).  
 [22] L. Wolfenstein, *Phys. Rev. D* **17**, 2369 – 2374 (1978).  
 [23] S. P. Mikheev and A. Smirnov, *Yad. Fiz.* **42**, 1441 (1985).  
 [24] P. Siwach, K. Harrison, and A. B. Balantekin, *Phys. Rev. D* **108**, 083039 (2023).  
 [25] C. A. Argüelles and B. J. P. Jones, *Phys. Rev. Res.* **1**, 033176 (2019).  
 [26] M. J. Molewski and B. J. P. Jones, *Phys. Rev. D* **105**, 056024 (2022).  
 [27] B. Hall, A. Roggero, A. Baroni, and J. Carlson, *Phys. Rev. D* **104**, 063009 (2021).  
 [28] K. Yeter-Aydeniz, S. Bangar, G. Siopsis, and R. C. Pooser, *Quant. Inf. Proc.* **21**, 84 (2022).  
 [29] C. Noh, B. M. Rodríguez-Lara, and D. G. Angelakis, *New J. Phys.* **14**, 033028 (2012).  
 [30] V. Amitrano, A. Roggero, P. Luchi, F. Turro, L. Vespucchi, and F. Pederiva, *Phys. Rev. D* **107**, 023007 (2023).  
 [31] M. Ila and M. J. Savage, *Phys. Rev. Lett.* **130**, 221003 (2023).  
 [32] G. D. Molfetta and A. Pérez, *New J. Phys.* **18**, 103038 (2016).  
 [33] A. Mallick, S. Mandal, and C. M. Chandrashekar, *Eur. Phys. J. C* **77**, 85 (2017).  
 [34] I. Esteban, M. C. Gonzalez-Garcia, M. Maltoni, T. Schwetz, and A. Zhou, *J. High Energy Phys.* **2020**, 178 (2020).  
 [35] R. Acciarri and et. al., (2016), arXiv:1601.05471 [physics.ins-det].  
 [36] M. Kobayashi and T. Maskawa, *Progress of Theoretical Physics* **49**, 652 (1973), <https://academic.oup.com/ptp/article-pdf/49/2/652/5257692/49-2-652.pdf>.  
 [37] S. Chaturvedi and N. Mukunda, *International Journal of Modern Physics A* **16**, 1481 (2001),



<https://doi.org/10.1142/S0217751X01003196>.

- [38] Arvind, K. S. Mallesh, and N. Mukunda, *Journal of Physics A: Mathematical and General* **30**, 2417 (1997).
- [39] S. Dogra, K. Dorai, and Arvind, **51**, 045505 (2018).
- [40] A. K. Jha, A. Chatla, and B. A. Bambah, *Eur. Phys. J. Plus* **139**, 68 (2024).
- [41] C. Giunti and C. W. Kim, *Fundamentals of Neutrino Physics and Astrophysics* (Oxford University Press, 2007).
- [42] C. Giganti, S. Lavignac, and M. Zito, *Prog. Part. Nuc. Phys.* **98**, 1 (2018).
- [43] S. Bilenky and B. Pontecorvo, *Phys. Rep.* **41**, 225 (1978).
- [44] A. Ioannisian and S. Pokorski, *Phys. Lett. B* **782**, 641 (2018).
- [45] H. C. Nguyen, B. G. Bach, T. D. Nguyen, D. M. Tran, D. V. Nguyen, and H. Q. Nguyen, *Phys. Rev. D* **108**, 023013 (2023).
- [46] M. Gonzalez-Garcia and M. Maltoni, *Phys. Rep.* **460**, 1 (2008).
- [47] S. Parke, *Phys. Rev. D* **93**, 053008 (2016).
- [48] S. Gariazzo, C. Giunti, M. Laveder, Y. F. Li, and E. M. Zanarin, *J. Phys. G: Nucl. Part. Phys.* **43**, 033001 (2016).
- [49] I. S. Oliveira, T. J. Bonagamba, R. S. Sarthour, J. C. Freitas, and E. R. deAzevedo, in *NMR Quantum Information Processing* (Elsevier Science B.V., Amsterdam, 2007) pp. 137–181.
- [50] A. Uhlmann, *Rep. Math. Phys.* **9**, 273 (1976).
- [51] R. Jozsa, *J. of Mod. Opt.* **41**, 2315 (1994).
- [52] A. Gaikwad, Arvind, and K. Dorai, *Quant. Inf. Proc.* **20** (2021).
- [53] H. Singh, Arvind, and K. Dorai, *Phys. Rev. A* **95**, 052337 (2017).
- [54] N. Khaneja, T. Reiss, C. Kehlet, T. Schulte-Herbrüggen, and S. J. Glaser, *J. Magn. Reson.* **172**, 296 (2005).
- [55] Z. Tošner, T. Vosegaard, C. Kehlet, N. Khaneja, S. J. Glaser, and N. C. Nielsen, *J. Magn. Reson.* **197**, 120 (2009).
- [56] G. Singh, K. Dorai, and Arvind, *Quant. Inf. Proc.* **22**, 394 (2023).
- [57] A. Singh, Arvind, and K. Dorai, *Phys. Rev. A* **94**, 062309 (2016).
- [58] O. G. Miranda and H. Nunokawa, *New J. Phys.* **17**, 095002 (2015).